Influences of Skull Segmentation Inaccuracies on EEG Source Analysis

B. Lanfer*[ab], M. Scherg[b], M. Dannhauer[c], T. R. Knösche[c], M. Burger[d] and C. H. Wolters[a]

*Corresponding author

[a] Institute for Biomagnetism and Biosignalanalysis
Westfälische Wilhelms-Universität Münster,
Malmedyweg 15, 48149 Münster, Germany
Email: benjamin.lanfer@uni-muenster.de
Phone: +49 251 83-52413
Fax.: +49 251 83-56874

[b] BESA GmbH
Freihamer Straße 18, 82166 Gräfelfing, Germany

[c] Max Planck Institute for Human Cognitive and Brain Sciences
Department of Neuropsychology
Stephanstraße 1A, 04103 Leipzig, Germany

[d] Institut für Numerische und Angewandte Mathematik
Westfälische Wilhelms Universität Münster
Einsteinstrasse 62, 48149 Münster, Germany

Abstract

The low-conducting human skull is known to have an especially large influence on electroencephalography (EEG) source analysis. Because of difficulties segmenting the complex skull geometry out of magnetic resonance images, volume conductor models for EEG source analysis might contain inaccuracies and simplifications regarding the geometry of the skull. The computer simulation study presented here investigated the influences of a variety of skull geometry deficiencies on EEG forward simulations and source reconstruction from EEG data.

Reference EEG data was simulated in a detailed and anatomically plausible reference model. Test models were derived from the reference model representing a variety of skull geometry inaccuracies and simplifications. These included erroneous skull holes, local errors in skull thickness, modeling cavities as bone, downward extension of the model and simplifying the inferior skull or the inferior skull and scalp as layers of constant thickness. The reference EEG data was compared to forward simulations in the test models, and source reconstruction in the test models was performed on the simulated reference data. The finite element method with high-resolution meshes was employed for all forward simulations.

It was found that large skull geometry inaccuracies close to the source space, for example, when cutting the model directly below the skull, led to errors of 20 mm and more for extended source space regions. Local defects, for example, erroneous skull holes, caused non-negligible errors only in the vicinity of the defect. The study design allowed a comparison of influence size, and guidelines for modeling the skull geometry were concluded.

Keywords

Skull modeling; EEG; Forward problem; Source reconstruction; Finite element model

Introduction

The inverse problem of reconstructing the sources of measured EEG data always involves solving the so-called forward problem; that is, the simulation of the potentials at the EEG electrodes for a given current density distribution (Sarvas, 1987, de Munck et al., 1988) by solving the quasi-static approximation of Maxwell's equations (Plonsey and Heppner, 1967, Sarvas, 1987). Exact analytical solutions for these equations only exist for simple geometries, like multi-shell spheroids (de Munck, 1988, Berg and Scherg, 1994, Irimia, 2005). Because these analytical solutions can be very efficiently evaluated, these models are still often used in spite of the fact that they do not very accurately account for the shape and the inner structure of the head.

As shown, for example, in (Haueisen et al., 1995, Gencer and Acar, 2004, Ramon et al., 2004, Güllmar et al., 2010, Wendel et al., 2008, Wendel et al., 2009, Acar and Makeig, 2010, McVeigh et al., 2007), it is often advisable to use more realistic models, which is only possible using advanced numerical methods. In the last decade, forward solutions based on the boundary element method (BEM) (Kybic et al., 2005, Acar and Makeig, 2010), the finite difference method (FDM)(Hallez et al., 2005) and the finite element method (FEM)(Bertrand et al., 1991, Buchner et al., 1997, Wolters et al., 2007a, Awada et al., 1997, Gencer and Acar, 2004, Marin et al., 1998) have been developed. For these solutions, it is important that the *numerical error*, often evaluated in studies with spherical volume conductor models where exact analytical solutions are available (see, e.g., (Kybic et al., 2005, Meijs et al., 1989, Wolters et al., 2007b, Wolters et al., 2007a)), and the *model errors* (see, e.g., (Bruno et al., 2004, Dannhauer et al., 2011, Haueisen et al., 1995, Li et al., 2007, Ramon et al., 2004)) are both as low as possible in order to achieve an acceptable *overall forward modeling error*. In addition, the computational complexity of these methods must be low enough so that forward simulations can be performed reasonably fast.

Individual, realistic head models for EEG source analysis, which describe the electrical properties

of the subject's head for the solution of the forward problem, are most often created by segmenting the head into regions of different tissue types and then assigning conductivity values to each of the regions. Model errors can arise from inaccurate segmentation of the regions (e.g., skull, brain) – known as geometry errors - or by using wrong values for the tissue conductivities. Note, however, that on top of these principally avoidable errors, the inherent simplifications of these compartment models cause errors, since in reality the conductivity is different at every point of the head.

Even if significant progress has been made, for example, in electrical impedance tomography (EIT) for the human head (Abascal et al., 2008), in practice, the determination of absolute values for tissue conductivities remains difficult. Therefore, conductivity values that were measured experimentally on tissue samples and published in the literature are used. Unfortunately, measured values for tissue conductivities can differ greatly between studies and even between tissue samples within the same study. See, for example, the values reported for the compact bone conductivity in (Law, 1993) and (Akhtari et al., 2002).

The skull plays a special role in modeling the volume conductor (Hämäläinen et al., 1993, Sadleir and Argibay, 2007, Dannhauer et al., 2011). Its conductivity is an order of magnitude smaller than the conductivity of other brain tissues and it is situated between the source space and the sensors. Therefore, errors in modeling the skull geometry have a potentially large effect on the solution of the EEG forward problem.

Model errors caused by different ways of modeling the skull conductivity were investigated by Dannhauer et al. (Dannhauer et al., 2011). The skull consists of layers of compact bone encasing a layer of cancellous bone, whose thickness varies over the skull. On average, the conductivity of the compact bone has been measured to be a factor of 3.6 lower than that of the cancellous bone (Akhtari et al., 2002). Large effects were found when approximating the skull as one compartment with homogeneous isotropic or anisotropic conductivity. The authors conclude that, if compact and cancellous bone can be identified with sufficient accuracy and their conductivities can be assumed

to be known, they should be modeled explicitly by assigning either compact or cancellous bone conductivity to each voxel.

While it is clear that many individually variable features of the head play a crucial role in the forward modeling of EEG/MEG, individual head model generation, and especially modeling the complex skull geometry, is still not a trivial task in practice. One important reason for this is that in many applications, T1 weighted magnetic resonance images (MRIs) are the only modality available for anatomical information. These MRIs are suboptimal for skull segmentation because they show low contrast between the skull and surrounding tissues. Moreover, many of the practically used MRIs, especially in clinical environments, suffer from low signal-to-noise ratio, especially in inferior regions of the head, and artifacts, for example, the water-fat-shift or the shading artifact. In addition, the resolution of commonly available MRIs is often quite low when compared to the size of the relevant anatomical structures, for example, the compact bone layers. Therefore, segmentation methods using MRIs as input data might produce results with geometric errors. Because of the thinness of the skull and its sub-layers, this structure is most vulnerable to such errors and often simplifications have to be applied. Therefore, and due to the important role of the skull, in this study, we will focus on the impact of unintentional (errors) and intentional (simplification) inaccuracies in skull models on forward solution and source localization accuracy.

A commonly occurring type of skull geometry inaccuracies comprises holes and local errors in skull thickness. A problem in segmenting the skull is the intricate internal structure of the bone. Due to noise, low resolution on the order of magnitude of the compact bone thickness, and water-fat-shift artifacts, it might be that a segmentation algorithm is not able to discern the thin compact bone layer and to differentiate between cancellous bone and the surrounding muscle or brain tissue, which do have similar intensities in the MRI. Erroneous labeling of compact and cancellous bone as scalp or brain tissue would lead to a locally underestimated skull thickness or, in extreme cases, even holes. In T1-weighted images, where there is nearly no contrast between compact bone and cerebrospinal

fluid (CSF), it might be that CSF is erroneously modeled as skull, which then would lead to a head model with locally overestimated skull thickness.

Besides these unintentional errors, intentional simplifications of the skull geometry play a role. Such simplifications might be necessary, for example, for the sinus cavities, as commonly available MRIs show nearly no contrast between air and compact bone, and therefore do not allow the shape and position of the sinus cavities to be determined.

Further simplifications are often necessary when modeling the skull base. The geometry of the skull base is quite complicated. It is very thin above the orbitae and very thick where it encases the sinus cavities. In addition, the signal-to-noise ratio in inferior regions of the head is often reduced, for example, due to MR coil sensitivity. It is therefore almost impossible to automatically and accurately segment the complicated geometry of the skull base, and simplifications are necessary.

Another interesting aspect concerning the generation of individual volume conductor models is the modeling of the inferior head regions. Here, segmentation is especially hard due to a limited field-of-view, a low signal-to-noise ratio and the complex anatomy in these regions. Simplifications, for example, cutting the model along an axial plane below the skull or modeling the inferior parts as an homogeneous region with a single conductivity value, might thus be necessary.

Because of the great importance of the skull in realistic volume conductor modeling, previous studies have already dealt with the influence of skull geometry defects on the EEG. Bénar et al. (Benar and Gotman, 2002) performed simulations using the BEM to investigate the effect of burr holes in the skull on source reconstruction. Localization errors of up to 20 mm caused by a burr hole were found, depending on location and orientation of the simulated source. Another study concerning the influence of a skull hole on the EEG was conducted by Vanrumste et al. (Vanrumste et al., 2000), who performed simulations in spherical volume conductors and found large localization errors when the hole was not incorporated into the volume conductor. Further investigations on the influence of skull holes on the EEG with similar results can also be found in

the literature (van den Broek et al., 1998, Li et al., 2007, Oostenveld and Oostendorp, 2002).

Effects of local errors in skull thickness are also dealt with in previous studies (Cuffin, 1993, Roche-Labarbe et al., 2008, Yan et al., 1991), pointing out the sensitivity of EEG source analysis to this specific parameter. In (Bruno et al., 2003, Bruno et al., 2004) the influence of the downward extension of the volume conductor was studied and large errors were reported when the model was cut at a plane intersecting the inferior part of the skull.

Results of previous studies on the influence of different skull geometry deficiencies cannot be compared directly, as many aspects of the designs of the studies differ. Volume conductors with different levels of detail are used: Some studies employ spherical three layer models, others use three compartment realistically shaped models incorporating the scalp, skull, and brain, and only a few use more detailed, realistic models. Furthermore, studies differ in, for example, their choice of conductivities for the volume conductor model and in the placement and number of electrodes.

In the computer simulation study presented here, the influence of a wide range of skull geometry deficiencies on the EEG forward simulation and source reconstruction are investigated, including skull holes, local errors in skull thickness, sinus cavities modeled as compact bone, the downward extension of the volume conductor model, simplification of the inferior skull and modeling the inferior skull and scalp as layers of constant thickness. A detailed and anatomically plausible reference model with 1 mm geometry-adapted hexahedral finite element meshes and the accurate FEM (Rullmann et al., 2009, Wolters et al., 2007b)are employed for the generation of reference EEG data. Forward simulation and source reconstruction errors in test models representing the skull geometry deficiencies are evaluated for probe sources across the whole brain volume. Finally, based on the comparable results found for the influences of a range of skull geometry deficiencies, we are able to draw guidelines on how to model the skull geometry for the generation of accurate individual volume conductor models. Segmentation procedures can be designed and evaluated taking these guidelines into account.

Materials and Methods

Study Setup

We constructed a detailed and anatomically plausible volume conductor model from MR data, which we refer to as *reference model* throughout this work. Using forward simulation methods in the reference volume conductor model, the potentials at a set of scalp electrodes, generated by a specified dipole source within the brain, can be computed. This is our reference data. Here we assume that the reference data are representative for real EEG data, as would be measured during actual experiments. Test models representing skull geometry defects and simplifications were derived from the reference volume conductor model.

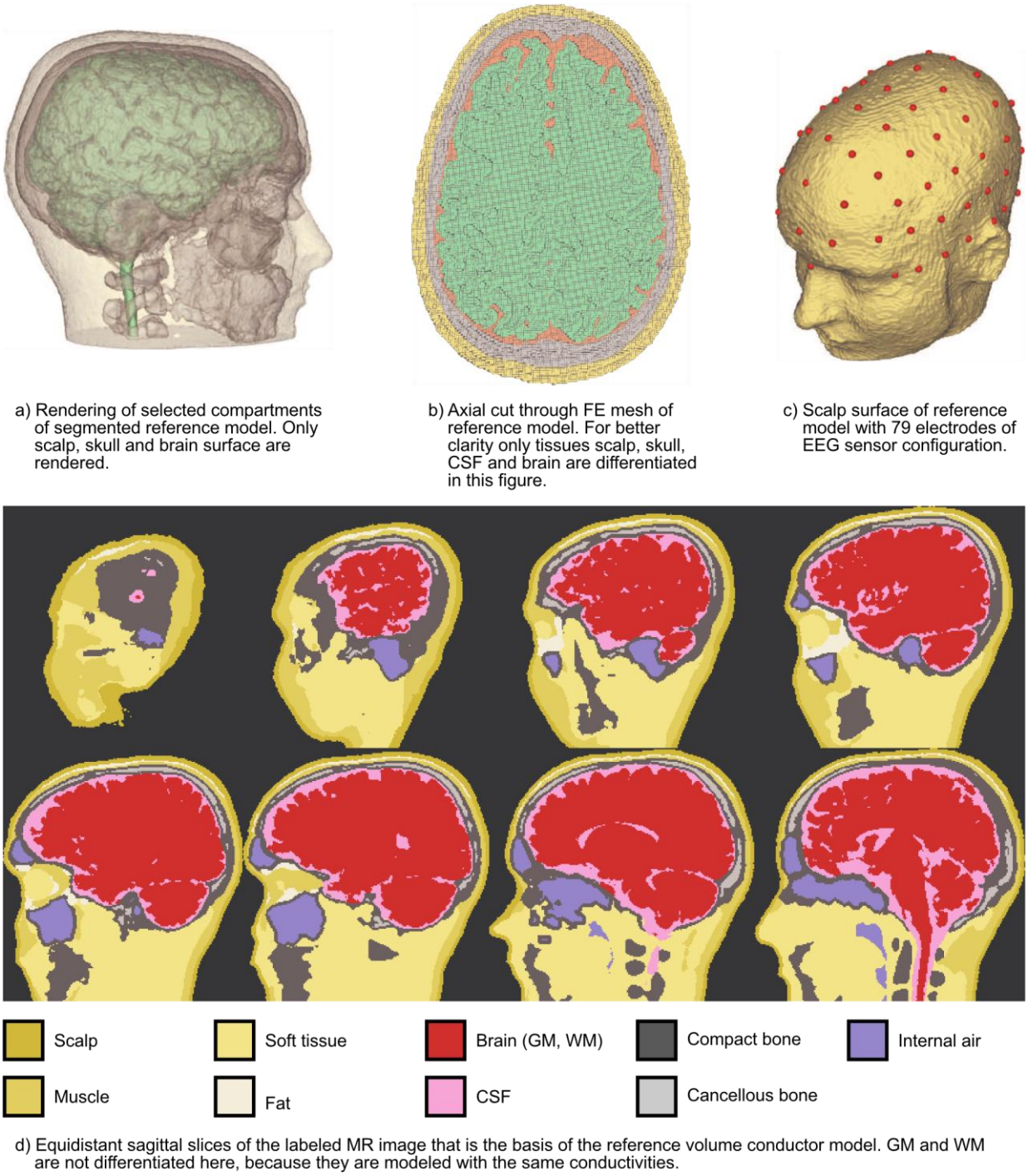

Figure 1 *Rendering of segmented reference model, cut through reference FE mesh, EEG sensor configuration and slices of labeled reference image.*

The presented study can be approximately divided into two parts. In the first part, influences of the skull segmentation deficiencies on the *forward simulation* were investigated. For this purpose, the reference potentials for a large set of single dipole probe sources were computed. For the same set of probe sources, the potentials were simulated with each of the test volume conductors. The test

and the reference potentials were compared for each source individually. Error measures, which were used for the quantification of the potential differences, are described below.

The second part of our study investigated the effects of skull modeling deficiencies on *inverse source reconstruction*. Again, for a large number of single dipole probe sources, the reference potentials were generated by performing forward simulations in the reference volume conductor model. Then, for each of the probe sources individually, an inverse method was applied to reconstruct the probe sources from the reference EEG data. The forward simulations on which the inverse method relied were performed in the test models. The differences between the reference and the reconstructed source locations were evaluated.

To illustrate the dependency of the forward and inverse errors on the position of the source inside the volume conductor and relative to the skull defect, error maps were plotted. Errors for sources at the same position, but with different orientations were averaged. Sources were located on the nodes of a regular cubic grid, and in Figures 3, 5, and 6 errors for slices through this cubic grid are presented. The errors were overlaid onto slices of the test model for which the errors were calculated.

Furthermore, errors were analyzed using descriptive statistics, giving information about the maximal and mean errors, as well as the proportion of affected sources. Most importantly, effect sizes were compared in order to derive a modeling guideline.

Construction of Reference and Test Models

The reference model was segmented in a semi-automatic way from a set of co-registered MRIs of the same subject. Also incorporating a CT image into the labeling procedure would have been advantageous, especially with regard to skull segmentation. However, such a dataset including a suitable CT image and suitable MR images, meeting all the criteria discussed below, was not available for this study. A T1-weighted image with fat suppression using selective water excitation (3D TFE sequence, TR 9.32ms, TE 4.45ms), a T1-weighted image with minimal water-fat-shift (3D

TFE sequence, TR 4.05ms, TE 1.81ms, bandwidth 777 Hz) and a T2-weighted image (2D SE sequence, TR 5460ms, TE 60ms) were used. All images were acquired on a Philips 3T MRI scanner and at an original resolution of 1.17 x 1.17 x 1.17mm³. Images were resampled to 1.0mm³ isotropic resolution before labeling. Coregistration of the multimodal MR images was performed using an affine registration approach with mutual information as cost function (Wells et al., 1996). Only tissue types with significantly different conductivities were differentiated. Segmentation of the reference model was done as follows.

A mask marking the intracranial space, here called brain mask, was created by thresholding the T2-weighted image. The surface of this mask was further smoothed by applying suitable morphological operations and fitting a deformable surface model to it. The T1-weighted image was masked with the brain mask and the tissues cerebro-spinal fluid (CSF), gray matter (GM) and white matter (WM) were identified using the classification provided by the *FSL FAST* software tool (Zhang et al., 2001). An alternative approach to generate a suitable initial brain mask would have been to use FSL's *Brain Extraction Tool (BET)* (Smith, 2002).

For the segmentation of the skull, the regions in the T1-weighted image which were not marked in the brain mask were classified into separate classes by their gray values. Voxels in dark gray value classes that approximately corresponded to compact bone were selected to form a first mask of the cranial skull. Morphological operations, that is, first a closing and then filling of holes, were applied to the cranial skull mask, complemented by some manual corrections. Skull openings for the optic nerves were labeled manually. To segment the cancellous bone, the T1-weighted image with minimal water-fat-shift was masked with the skull mask and thresholded to extract the bright regions inside of the skull where the diploe layer is situated. The minimal water-fat-shift in the MRI is an important requirement. In MRIs with significant water-fat-shift, the signal from the fatty tissue in the diploe layer is not displayed at the right location, but shifted in one direction. This would lead to an erroneously shifted diploe layer in the labeled segmentation. Masking of the cancellous bone

mask with a skull mask that was eroded by 2 mm was performed to guarantee a minimum thickness for the inner and outer compact bone layer.

Bone structures and air-filled cavities in the inferior part of the head were labeled by first selecting the low-intensity gray value classes in the inferior regions of the T1-weighted image (i.e., at a certain minimum distance to the segmented brain mask). Morphological operations, for example, opening operations, and manual corrections were then performed to separate bone structures and air-filled cavities. Some inferior structures, for example, the vertebrae and the sinus cavities, were labeled completely by hand.

The remaining regions of the head that were not yet labeled as bone, air-filled cavities or brain were segmented into the tissues scalp, muscle, fat and soft tissue. Fatty tissue was identified by selecting bright regions in the T1-weighted image with minimal fat-shift. Muscle and scalp tissues were segmented by choosing the corresponding classes from the gray value classification of the non-brain tissue. A minimum thickness of 2 mm was guaranteed for the scalp layer by labeling all voxels at a distance of 2 mm or less from the head surface as scalp. In a similar way, a minimum thickness of 2 mm was also ensured for the superior muscle layer Voxels in the inferior head with medium gray values in the T1-weighted image were labeled as soft tissue.

The complete labeled volume was composed from the tissue masks, and manual corrections were applied to the final segmentation. The resulting labeled segmentation image of 1.0 x 1.0 x 1.0 mm^3 resolution was found to be detailed and anatomically plausible (Figure 1d). A rendering of the surfaces of the compartments skin, skull and brain of the reference volume conductor model is presented in Figure 1a.

Test models (TM) representing the different skull segmentation deficiencies were derived from the reference segmentation. Table 1 lists the test models that were investigated in this study. The first test model series – test model 1c is shown in Figure 2a – was constructed by introducing holes of varying sizes in the left-temporal skull. Location of the skull hole was not varied, as we expect

qualitatively similar errors for holes in other areas of the calvaria. Electrode coverage, for example, which might influence the errors, is similarly good for all areas of the skull cap. Holes were modeled by filling them with material of the same conductivity as muscle tissue.

The influence of local under- or overestimation of skull thickness is investigated in the second test model series, where the thickness of the skull was either increased or decreased by a varying amount in a circular region of 20 mm diameter. Test model 2f with decreased skull thickness is presented in Figure 2b.

In a third set of test models (Figure 2c), all sinuses except the frontal one or all sinuses without exception were modeled as compact bone. Sinuses were filled with air in the reference model.

The fourth series of test models investigated the influence of the downward extension of the model. Therefore, test models were created by cutting the reference model along an axial plane at distances of 0, 20 and 40 mm, respectively, below the occipital hole of the skull. Test model 4d was also cut 40 mm below the skull, but in addition, the model was further simplified. In that model, sinuses were modeled as compact bone (as in test model 3b) and all inferior areas (i.e., areas below a plane passing approximately through nasion and inion and at a distance of more than 30 mm from the source space) were labeled as scalp tissue. A rendering of test model 4a from this series is presented in Figure 2d.

In the test models of the fifth series, the inferior skull (i.e., mainly the skull base) was approximated as a layer of 4, 6 and 8 mm constant thickness, respectively. See Figure 2e for a rendering of one of the test models from the series.

In the sixth set of test models, not only the inferior skull was approximated by a layer of 6 mm constant thickness, but also the inferior scalp was approximated by a layer of 4, 6 and 8 mm constant thickness. See Figure 2f for an illustration.

Test models 1 – Skull hole	**Test models 2 - Skull thickness**	**Test models 3 - Sinuses**	**Test models 4 - Downward extension**	**Test models 5 - Simplified inferior skull**	**Test models 6 - Simplified inferior skull and scalp**
Hole in left-temporal skull with varying diameter.	Skull too thick or too thin in skull region of 20 mm diameter.	Sinuses modeled as filled with compact bone instead of air.	Model cut along axial plane at varying distances below skull.	Inferior skull approximated by layer of constant thickness.	Inferior skull and scalp approximated by layers of constant thickness. Skull layer always with 6 mm constant thickness.
1a: 2 mm hole **1b**: 6 mm hole **1c:** 10 mm hole	**2a**: 2 mm thicker **2b**: 4 mm thicker **2c**: 6 mm thicker **2d**: 2 mm thinner **2e**: 4 mm thinner **2f**: 6 mm thinner	**3a**: All sinuses, except frontal sinus modeled as compact bone **3b**: All sinuses, without exception, modeled as compact bone	**4a**: Cut 0 mm below skull **4b**: Cut 20 mm below skull **4c**: Cut 40 mm below skull **4d:** Cut 40 mm below skull and further simplifications in inferior regions	**5a**: 4 mm constant skull thickness **5b**: 6 mm constant skull thickness **5c**: 8 mm constant skull thickness	**6a**: 4 mm constant scalp thickness **6b**: 6 mm constant scalp thickness **6c**: 8 mm constant scalp thickness

Table 1: Test models investigated in the present study. See text for additional details on test models.

The Finite Element Method

For our simulation study, we need to solve the forward problem in complex volume conductors with, for example, holes in the skull, and incorporating a large number of tissues with different conductivities. The FEM is known to be able to carry out these simulations with high accuracy and in sufficiently short computation times (Rullmann et al., 2009, Wolters et al., 2007b).

We used the Venant direct method (Buchner et al., 1997) for modeling the dipole source in the FE

head model, because it yielded suitable accuracy across all realistic source locations in multilayer sphere model validation studies (Wolters et al., 2007b, Lew et al., 2009).

Forward simulations and source reconstructions were performed for a large number of probe sources. To be able to do this, the *Transfer Matrix Approach* is employed, which speeds up the forward simulations for large numbers of sources (Wolters et al., 2004, Gencer and Acar, 2004).

Construction of Geometry-Adapted Hexahedral FEM Volume Conductor Models

Geometry-adapted hexahedral FE meshes deliver accurate results (in combination with an isoparametric FE approach) and are easily constructed from labeled MR images (Wolters et al., 2007b). In particular, hexahedral mesh generation is much more straightforward than surface-based meshing approaches often used for tetrahedral FEM or BEM modeling. The latter approaches require certain conditions to be fulfilled for the input surfaces. Some of these conditions, for example, that interfaces must not have self-intersections and must not intersect each other, are hard to fulfill in practice. In order to obtain sufficient accuracy, high resolution 1mm hexahedral meshes were constructed. Regular hexahedral meshes were generated by simply interpreting the 1x1x1 mm^3 cubic voxels of the labeled image as hexahedral elements. In an additional step, the so-called node-shift approach was then used to generate geometry adapted-hexahedral FE meshes, which are known to provide even better accuracy (Wolters et al., 2007b).

The resulting FE mesh for the reference volume conductor model consisted of around 3.56 million nodes and around 3.47 million elements. An axial slice through the reference FE mesh is presented in Figure 1b.

Isotropic conductivities were assigned to the elements. The conductivity values used for the different tissues in the volume conductor models are listed in Table 2.

Tissue	**Conductivity**	**Tissue**	**Conductivity**
Scalp	0.43 S/m (Haueisen et al., 1995)	Cancellous bone	0.021 S/m (Akhtari et al., 2002)
Muscle	0.11 S/m (Haueisen et al., 1995)	Internal air	0.0001S/m (Haueisen et al., 1995)
Fat	0.04 S/m (Haueisen et al., 1995)	Cerebro spinal fluid	1.79 S/m (Baumann et al., 1997)
Soft tissue	0.17 S/m (Haueisen et al., 1995)	Gray matter (GM)	0.33 S/m (Haueisen et al., 1995)
Compact bone	0.005 S/m (Akhtari et al., 2002)	White matter (WM)	0.33 S/m (Haueisen et al., 1995)

Table 2: Tissue conductivities used for the construction of the reference and test FE volume conductor models. Conductivity values were measured experimentally on tissue samples and can be found in the literature referenced.

Error Measures

To quantify the effects of skull segmentation deficiencies on the forward simulations and the source reconstruction, we employed the following error measures.

The error between the scalp potentials computed in the reference model and in the test models was expressed in terms of the *Relative Difference Measure* (RDM) and the *Magnitude Error* (MAG) (Meijs et al., 1989).

$$RDM = \left\| \frac{\varphi^{ref}}{\|\varphi^{ref}\|} - \frac{\varphi^{test}}{\|\varphi^{test}\|} \right\|$$

$$MAG = \frac{\|\varphi^{test}\|}{\|\varphi^{ref}\|}$$

φ^{ref} and φ^{test} are the reference and the test model potential vectors, respectively, and $\| \|$ represents the L_2 norm.

While the RDM quantifies differences in the topographic patterns of two (simulated) measurements, the MAG describes an overall difference in magnitude. The minimum and maximum values for the RDM are 0 and 2, respectively. The optimum value for the MAG is 1.

Source reconstruction results can be evaluated by computing the localization error, the error in orientation and the magnitude error. In our study, we only discuss the localization error. It is defined as the distance from the reference source position to the reconstructed source position. In addition, we plot arrows from the reference to the reconstructed source position to indicate the direction of the mislocalization.

To measure the size of an influence of a skull geometry defect, we defined the proportion of affected sources. Threshold values for the RDM and the localization error were specified and all sources with errors larger than these were regarded as affected. We chose a value of 0.1 as the threshold for the RDM and a distance of 5 mm as threshold for the localization error. From previous experience, errors above these chosen thresholds can be regarded as non-negligible. The proportion of affected sources was defined as ratio of the number of sources with errors above the threshold to the total number of probe sources. A larger proportion of affected sources indicates a more global influence of the skull geometry defect under investigation.

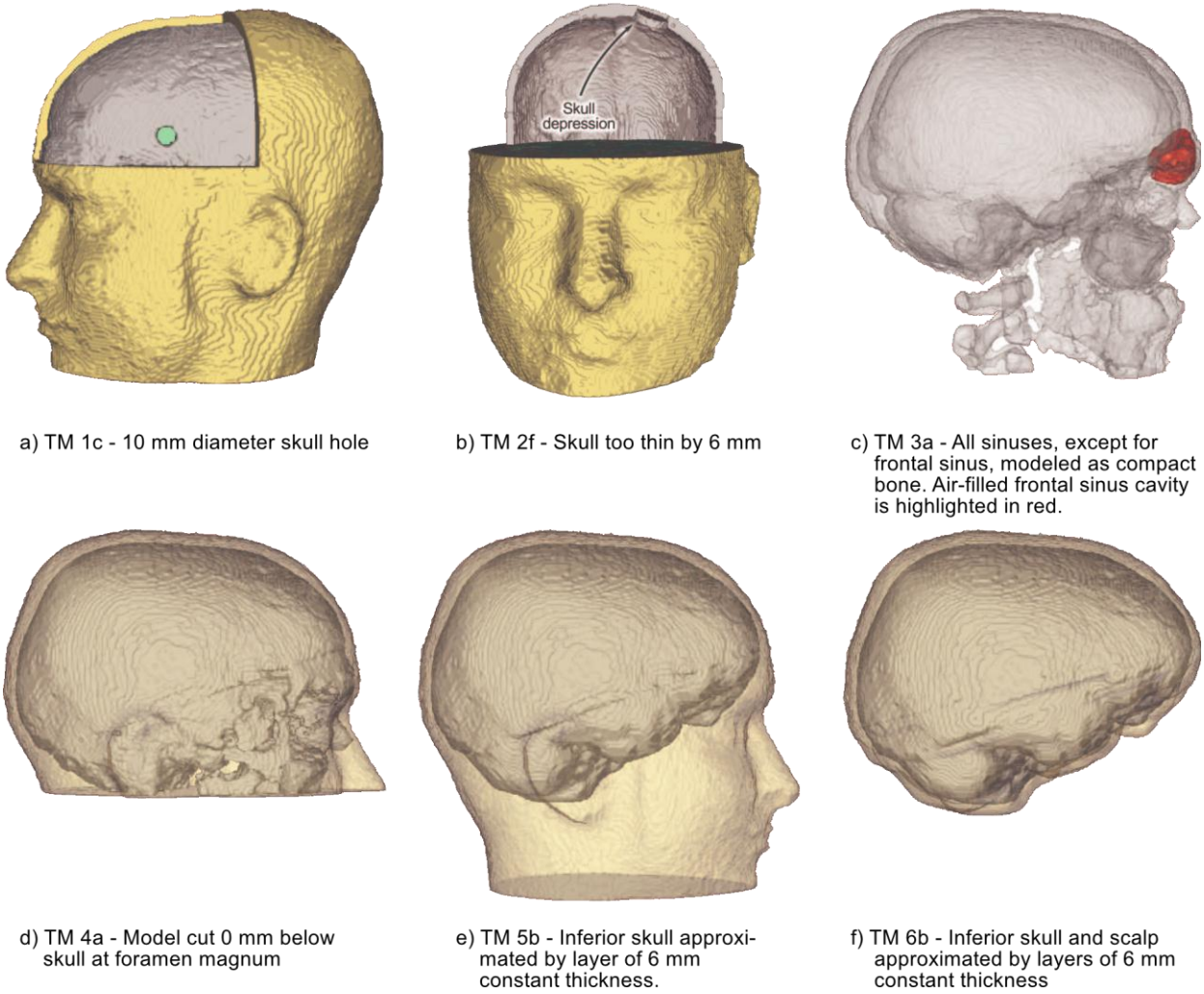

Figure 2 *Renderings of test models representing the skull geometry deficiencies investigated. Only selected tissue compartments are rendered to emphasize the skull geometry defect.*

Probe Sources, Electrode Configuration, Inverse Method

Influences on the forward simulations were investigated for probe sources on a regular cubic 4 mm grid. We took care to ensure that all sources were located inside the brain compartment and sufficiently far away from CSF or bone tissue so that, for each probe source, the closest node of the FE mesh only belongs to elements, which are labeled as brain. We refer to this condition as *Venant condition.* It must be fulfilled to avoid unrealistic source modeling and numerical problems for the Venant dipole modeling approach (Lew et al., 2009). At each source location, we placed three sources, oriented in x-, y- and z-direction, each with a magnitude of 1 nAm.

Reference sources for the source reconstruction investigations were distributed on a regular cubic

10 mm grid. Again, all source locations were situated inside the brain compartment and with sufficient distance to the other head compartments to fulfill the Venant condition. The influence on the source reconstruction might significantly depend on the orientation of the reference sources. Therefore, we put 10 sources at each source location with orientations regularly sampling one hemisphere. The magnitude of the reference sources was 1 nAm. Results were later averaged across these 10 source directions for visualization and to remove the dependence of the observed errors from the orientation of the dipole source.

The electrode configuration for our simulation studies was constructed by distributing 79 electrodes on the scalp surface of the reference model following the international 10-10 system (Nuwer et al., 1998). An illustration of the electrode configuration is presented in Figure 1c.

The robust Goal Function Scan method was our method of choice for source reconstruction from the reference potentials in the second part of the study. The scan was performed on a regular cubic grid of 1 mm isotropic resolution covering the entire brain compartment to achieve sufficient accuracy and the position of the grid node with the highest goal function value was interpreted as the reconstructed source position. We took care to ensure that the grid nodes had a sufficient distance to non-brain tissue to prevent numerical errors during source reconstruction. To avoid an inverse crime (Kaipio and Somersalo, 2007), the cubic grid was shifted by 0.5 mm in each direction relative to the grid on which the reference sources were placed so that no reference source was lying directly on a node of the scanning grid. This also means that a perfect localization is not possible in our study.

Computation Platform

All computations were carried out on a regular PC with an *Intel Core 2 Quad Q6600* processor and 8 GB of RAM using the *SimBio* toolbox (SimBio Development Group, 2011). Geometry-adapted hexahedral FE meshes were constructed using the software *VGrid (Hartmann and Berti, 2003).* Visualizations, for example, of the error maps, were done using *SCIRun (SCIRun, 2011).*

Results

Forward Simulations

Forward simulations for the set of probe sources were performed in the reference model and each of the test models. The simulated potentials were compared between the reference and the different test models and error measures were computed. RDM error maps for selected test models are presented in Figure 3. The distribution of absolute MAG errors was in general very similar to the RDM error distribution. Therefore, MAG error maps are omitted here and only the tendency to over- or underestimate potentials is discussed. For the interested reader the MAG error maps are provided in the supplementary materials.

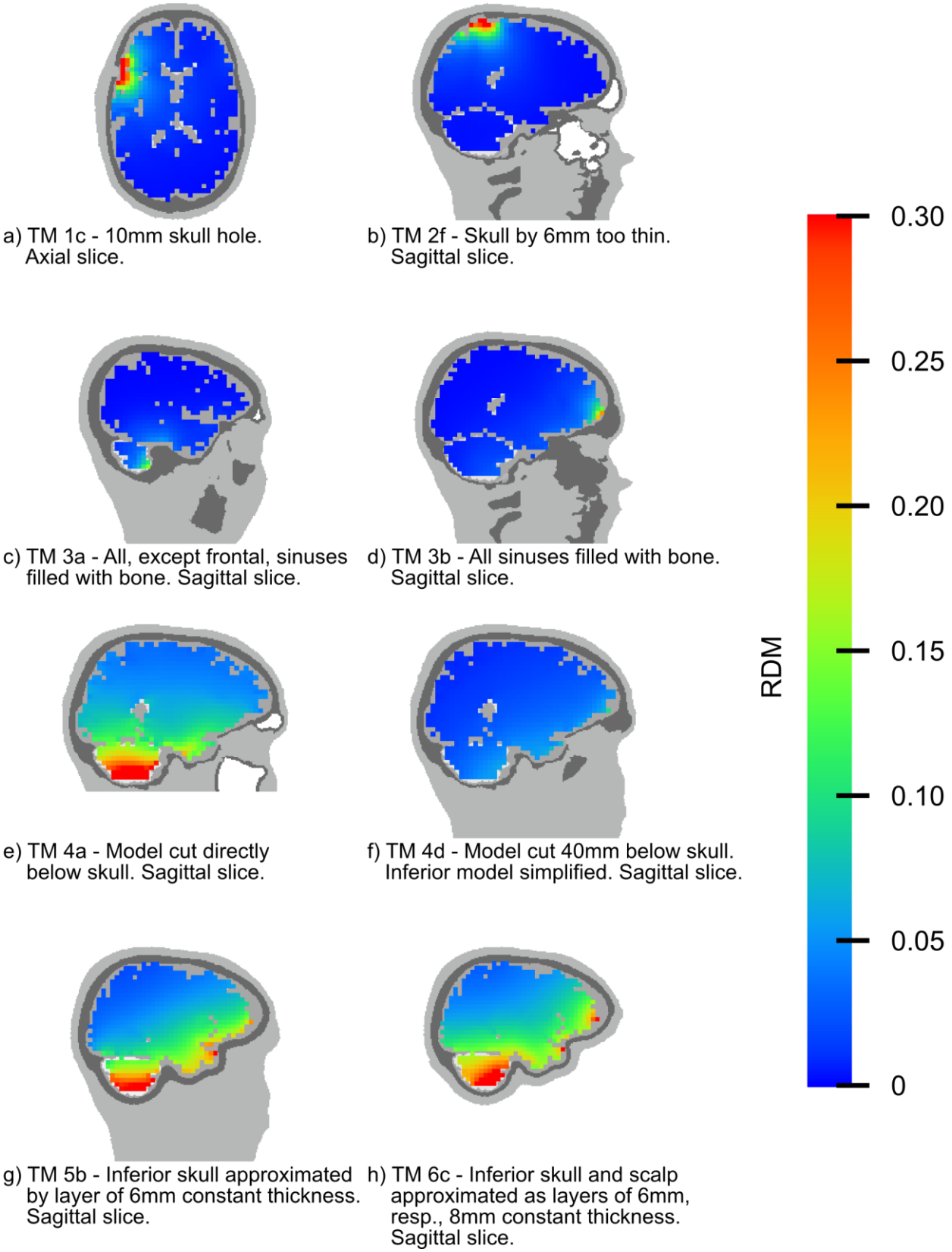

Figure 3 *RDM error maps for selected test models. Errors for sources at the same position, but with different orientations were averaged. Please note that the scaling of the error maps differs from the scaling of the comparison plots in Figure 4.*

For the test models with a **skull hole** of varying diameter, significant forward simulation RDM errors were only found for probe sources in a limited region around the skull hole (Figure 3a). MAG values larger than 1.0 were observed for probe sources close to the hole, indicating that the potentials computed in the test models were larger than the reference potentials.

The second test model series was derived by locally **increasing or decreasing the thickness** of the skull in a defined area. Significant RDM and MAG errors between the potentials computed in the test models and the reference potential were only found for probe sources in a region close to the modification (Figure 3b). MAG errors indicate that potentials computed in test models 2d to 2f, in which the skull thickness was decreased, were overestimated in comparison to the reference potentials.

In the third test model series, all **sinuses** and all sinuses except the frontal one were modeled as compact bone while the sinuses were filled with air in the reference model. For the case without frontal sinuses, results showed that RDM and MAG errors were noticeable only in inferior regions close to the skull base, where large sinus cavities are located (Figures 3c and 4). When the frontal sinuses were filled with compact bone, RDM and MAG errors could also be observed for frontal sources close to the skull (Figure 3d).

The models in the fourth test model series were constructed to investigate the effects of different methods of **downward extension** of the volume conductor model. Noticeable RDM and MAG errors were found for models 4a, 4b and 4d (Figures 3e, 3f and 4). For test model 4a, prominent errors were found for inferior sources in temporal and occipital regions (Figure 3), whereas for test model 4b, non-negligible errors were found only for sources in the cerebellum. The MAG error for these models indicated that the potentials in the test models were overestimated. In test model 4d, non-negligible errors were found for a limited number of sources in frontal and temporal regions (Figure 3f).

To investigate the influence of **simplifying the inferior skull**, test models 5a to 5c were constructed. Large RDM and MAG errors could be observed for sources close to the skull base as shown in the error maps in Figure 3g. RDM errors were maximal for cerebellar sources, sources in the temporal lobe close to the skull, where the optical nerve passes through the skull in the reference model, and for frontal sources, where the frontal sinuses are located and the skull in the reference model is thick (Figure 3g). The magnitude errors indicated that the potentials in all three test models were underestimated compared to the reference potentials.

The last set of test models was built to study the influence of **simplifying both the inferior skull and scalp** as layers of constant thickness. The observed distribution of the RDM error was similar to that observed for the test models with only the inferior skull simplified, but errors were generally larger, as can be seen in Figures 3h and 4. Largest RDM errors could be found for sources close to the base of the skull (Figure 3h). MAG error maps presented a slightly different picture. In the model with the thinnest scalp, the magnitude of the potentials was overestimated for nearly all sources. When the inferior scalp thickness was increased, the MAG error maps became more heterogeneous. At 8 mm inferior scalp thickness, in some regions, for example, in a part of the temporal lobe and the cerebellum, the potentials were overestimated, whereas in other regions, like the remaining part of the temporal lobe and in occipital regions, potentials were underestimated. In test model 6c, the effects on the magnitude of simplifying the inferior skull and the inferior scalp partly canceled each other out, and MAG errors for sources close to the skull base became negligible, for example, in temporal regions.

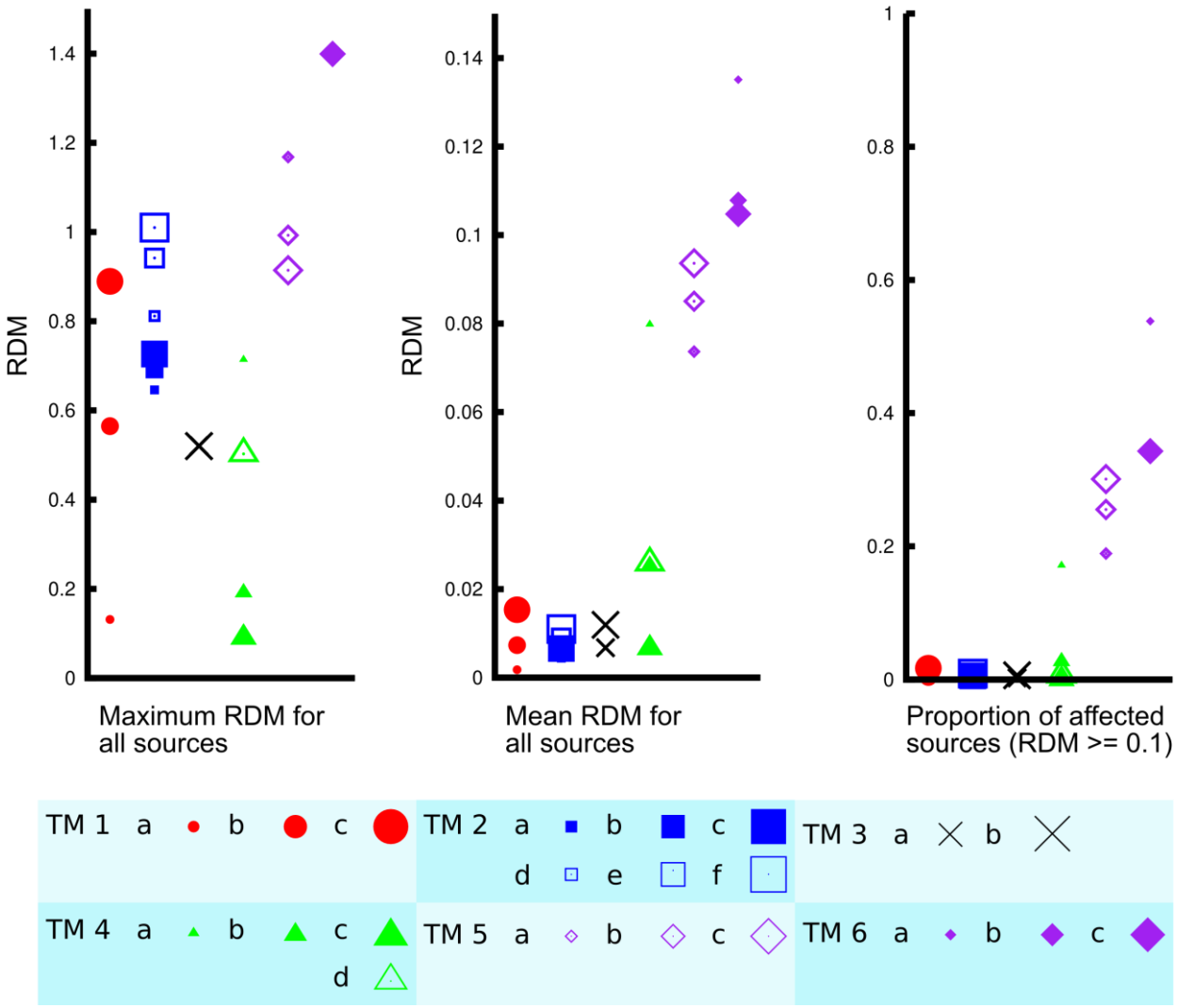

Figure 4 *RDM error characteristics for sources in cerebrum and cerebellum.*

Figure 4 shows the maximum RDM errors, the average RDM errors and the proportion of affected sources, as defined in subsection *Error Measures*, for all test models. Maximum errors, and also the proportion of affected sources, were computed without averaging the errors across source directions beforehand. As all influences were investigated in the same simulation setup, we could directly compare the influences.

Comparing the errors inside a test model series representing the same skull geometry error or simplification, we found increasing errors when increasing the diameter of the skull holes (TMs 1a-c), the change in skull thickness (TMs 2a-f), and the constant thickness of the inferior skull layer (TMs 5a-c). Errors decreased when increasing the distance of the cutting plane from the skull base

(TMs 4a-c) and the constant inferior scalp thickness (TMs 6a-c).

Of all test models, the mean RDM error is smallest in model 1a. The skull hole of only 2 mm diameter in this model only produced an observable error for sources very close to the hole. The mean RDM was also small for the other test models where the conductivity was changed in only a very limited region. These were the models with locally incorrect skull thickness and the models where the sinuses were modeled as compact bone. A small average RDM error, which we regard as negligible, was also found for the model which was cut 40 mm below the skull. Mean errors for the model cut 20 mm below the skull (test model 4b) and for the model cut 40 mm below the skull with additional simplifications of the inferior volume conductor (test model 4d) were only slightly larger. Large average RDM values of 0.07 and more when regarding sources in the cerebrum and the cerebellum could be found for the test model cut directly below the skull (test model 4a) and for the test models with simplified inferior skull (test models 5a-c) or simplified inferior skull and scalp (test models 6a-c). For these models, more than 17% of the sources are also affected (i.e., the RDM for more than 17% of all sources is larger than 0.1).

Source Reconstruction

In addition to the influence of the skull segmentation deficiencies on the forward solutions, we also investigated the influence on single dipole source reconstruction. In this subsection, we report the localization errors for the test models. Error maps showing localization errors and mislocalization tendencies are presented in Figures 5 and 6. An additional error map showing the mislocalization at each reference source position for the source orientation with the maximum localization error is provided in the supplementary materials.

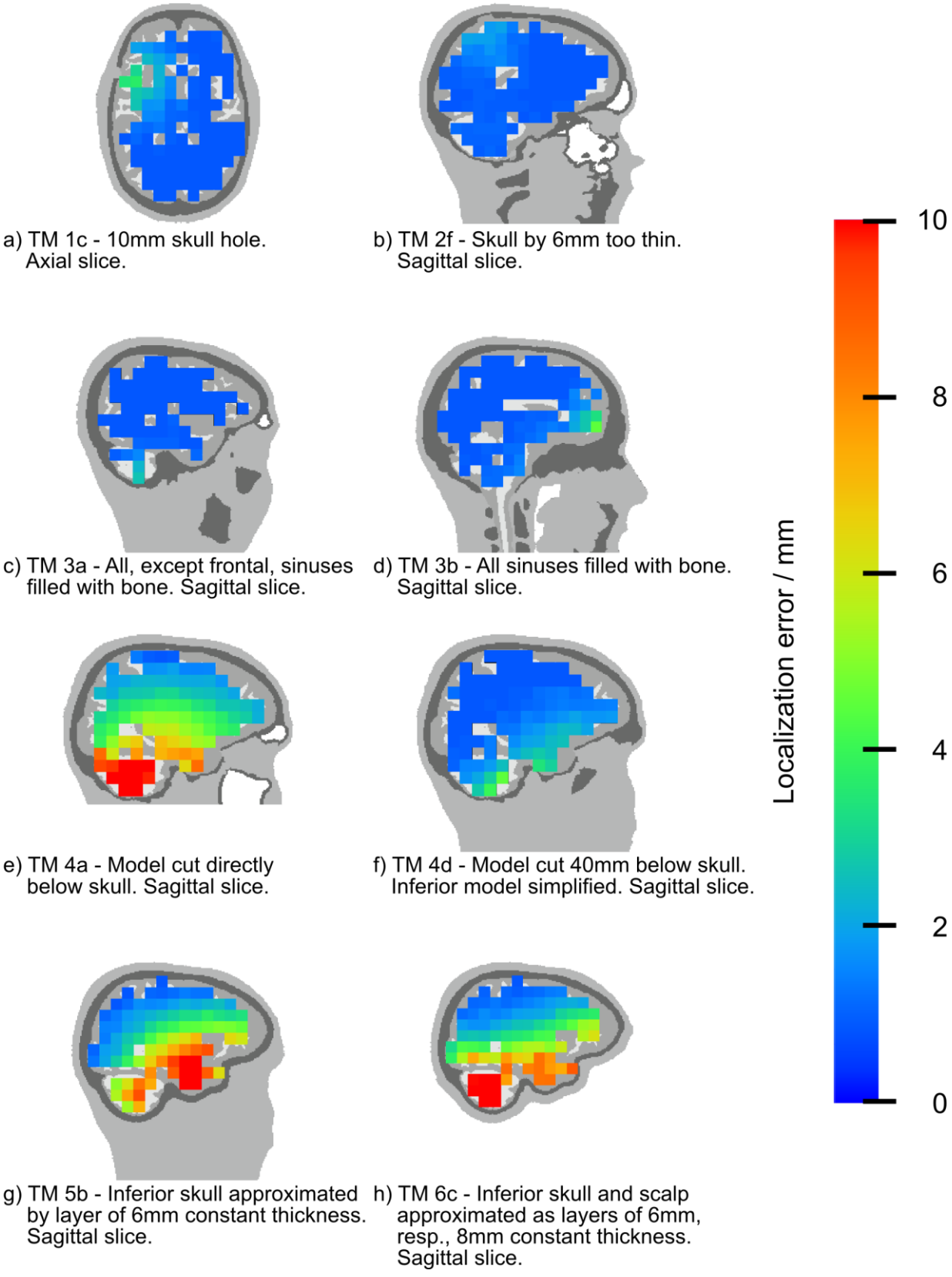

Figure 5 *Localization error maps for selected test models. Errors for sources at the same position, but with different orientations were averaged. Please note that the scaling of the error maps differs from the scaling of the comparison plots in Figure 7.*

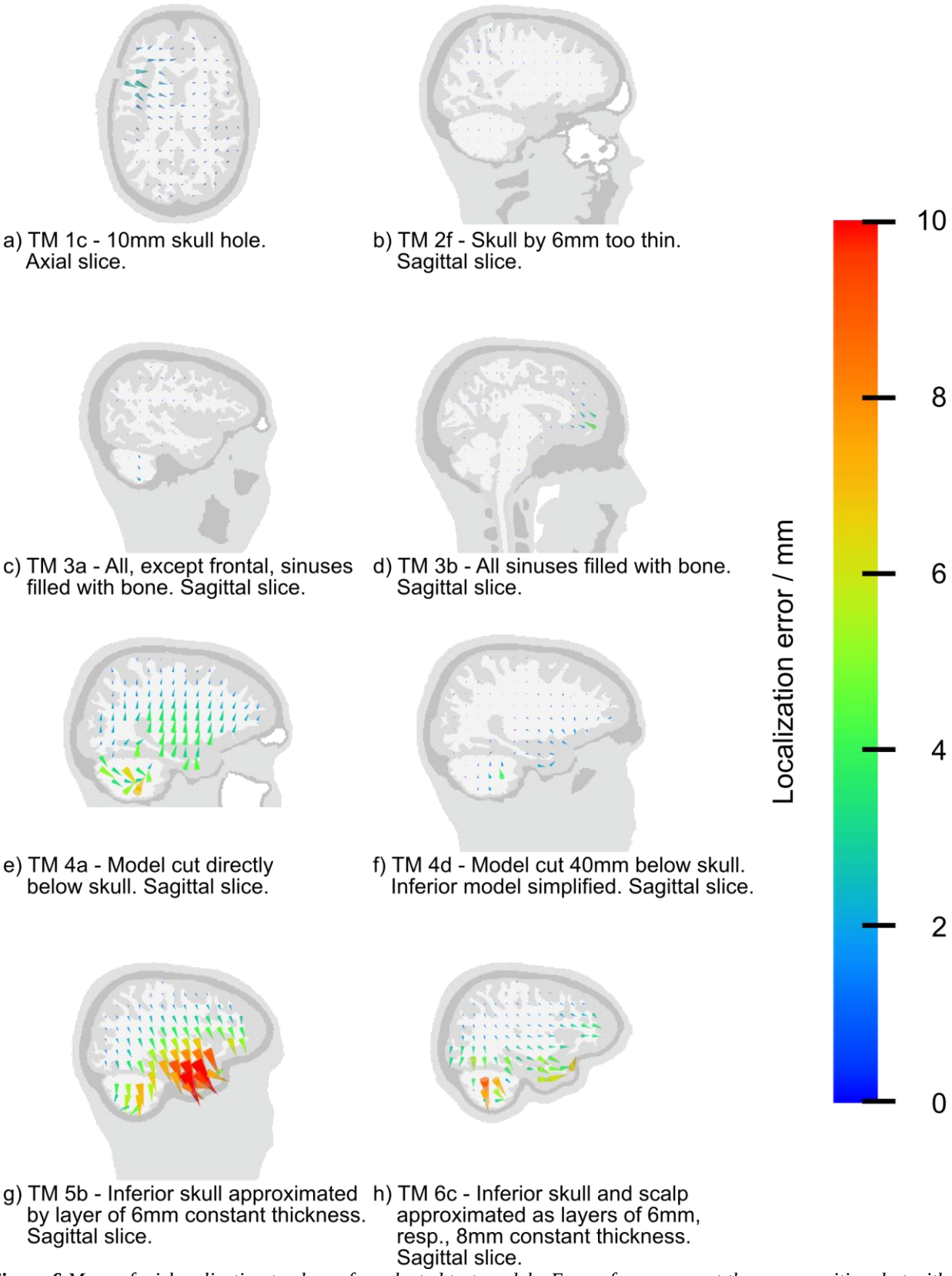

Figure 6 *Maps of mislocalization tendency for selected test models. Errors for sources at the same position, but with different orientations were averaged. The length of the cones is scaled by a factor of 3 to improve visibility of small mislocalization tendencies. Please note that the scaling of the error maps differs from the scaling of the comparison plots in Figure 7.*

For the test model series 1 with a **skull hole,** noticeable source reconstruction errors could only be observed for the two models with holes of 6 and 10 mm diameter and only for sources in the proximity of the skull hole (Figure 5a). Affected sources were reconstructed at positions lying deeper inside the head as compared to the reference positions (Figure 6a).

In the test model series 2 with **skull thickness errors,** only small localization errors were found. A localization error map for test model 2f is shown in Figure 5b. The few sources that were reconstructed with noticeable errors were situated in the vicinity of the skull thickness change. Due to the small size of the averaged mislocalization vectors, we could not make out a clear mislocalization tendency (Figure 6b). Nevertheless, for test model 2f we saw large mislocalizations occurring for some dipole orientations and that sources with these orientations are reconstructed farther away from the skull thickness defect.

Modeling the air filled **sinuses** as compact bone (test model series 3) only caused errors in the source reconstruction in areas close to the sinuses. When all sinuses except the frontal sinuses were modeled as bone, noticeable errors were found only for inferior sources in the cerebellum (Figure 5c). The maximum localization error for sources in the cerebrum when all sinuses except the frontal sinuses were ignored is well below 5 mm. When also modeling the frontal sinuses as bone, additional errors of up to 9 mm were found for a limited region in the frontal lobe directly adjacent to the frontal sinuses (Figure 5d). The affected frontal sources in test model 3b were reconstructed as being too deep when compared to the reference source positions (Figure 6d). We were not able to make out a consistent mislocalization tendency for the affected cerebellar sources.

Regarding the **downward extensions** of the volume conductor model (test model series 4), we found significant source reconstruction errors for inferior sources in the cerebellum and in the temporal lobe when cutting the model directly below the skull (Figures 5e, 6e, and 7). For single dipole orientations the localization errors clearly exceeded the averaged localization errors indicating that some particular dipole orientations are excessively affected by cutting the model

directly below the skull. When we cut the model 20 mm below the skull, non-negligible errors were mainly found for sources in the cerebellum. When the model was cut 40 mm below the skull, localization errors for all sources in the cerebrum were less than 4 mm. Non-negligible reconstruction errors were only found for a few sources in the cerebellum. Only small errors in the cerebellum and in temporal regions were found for test model TM 4d, where in addition to cutting the model 40 mm away from the skull, some simplifications in the inferior part of the head were introduced (Figures 5f and 6f). In test models TM 4a and 4b, where a non-negligible localization error could be observed, the mislocalization tendency for sources in the cerebrum was quite consistent. These sources were reconstructed too far superior (Figure 6e). The tendency for sources in the cerebellum was not as clear. Reference sources situated in a posterior region of the cerebellum were by trend reconstructed more anterior and partly more inferior.

The large RDM and MAG errors observed for the test model series 5 with **simplified inferior skull** translated to large source localization errors for source positions close to the base of the skull (Figures 5g, 6g, and 7) in our study. Localization errors reached values of around 24 mm. Sources throughout the brain were consistently mislocalized towards positions closer to the skull base as is illustrated in Figure 6g.

Finally, source reconstruction results for test model series 6 with **simplified inferior skull and scalp** were investigated. Large source reconstruction errors were found mainly for sources close to the base of the skull, especially for sources in the cerebellum and the temporal lobe (Figures 5h, 6h and 7). The mislocalization tendency was not consistent across the different models in this test model series (Figure 6h). It was consistent in test model TM 6a, where all sources were located too far superior. This tendency changed when the thickness of the simplified inferior scalp layer was increased. In model TM 6c, frontal sources were reconstructed too far anterior, and occipital and inferior sources were localized too far inferior. When comparing Figures 5h and 6h, it becomes obvious that in TM 6c, the mislocalization is also not consistent across dipole orientations. For

sources in the cerebellum, only a small mislocalization tendency can be made out because tendencies for individual dipole orientations cancel each other out (Figure 6h), while the averaged localization error is large (Figure 5h). We furthermore also directly observed large mislocalizations for single dipole orientations and sources in the cerebellum.

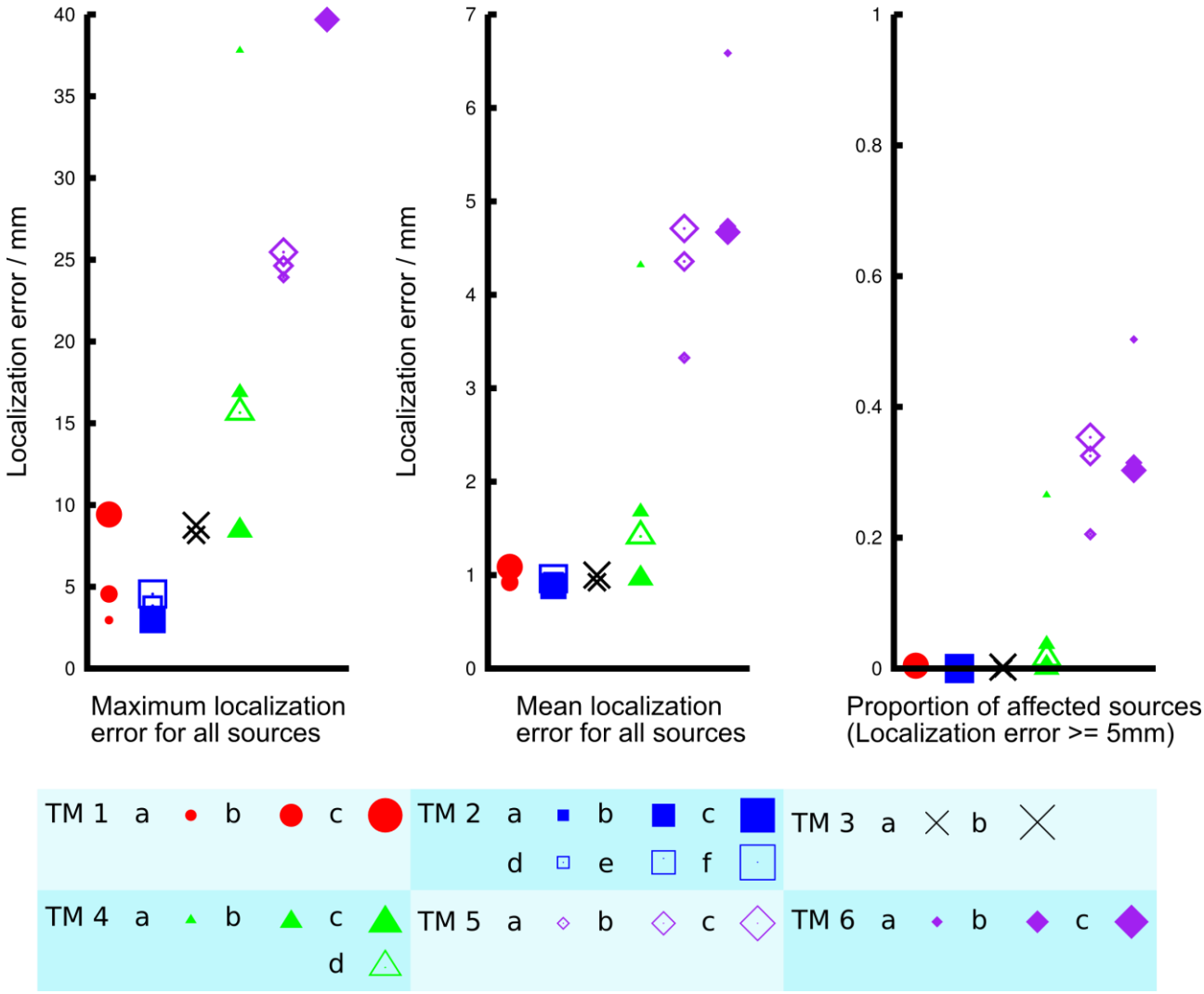

Figure 7 *Localization error characteristics for sources in cerebrum and cerebellum.*

In Figure 7 the maximum and mean localization errors as well as the proportion of affected sources (see subsection *Error measures* for definition) are presented for all test models. Maximum errors and the proportion of affected sources were computed without averaging across source directions beforehand. This allows us to compare the size of the effects investigated.

Comparing the localization errors inside a test model series representing the same geometry error or

simplification, we found the same trends as already reported for the forward errors.

Average localization errors for test models of the first three series – skull holes, incorrect skull thickness and sinuses modeled as compact bone – are close to the minimum error achievable with the inverse method used because of the local nature of these errors. Small average localization errors (less than 2.0 mm) are also found for models 4c and 4b (model cut 40 and 20 mm below the skull, respectively) and 4d (model cut 40 mm below skull with additional simplifications of inferior volume conductor). Cutting the model directly below the skull and simplifying the inferior skull, respectively, the inferior skull and scalp, caused on average larger localization errors exceeding 3.5 mm. In addition, for these models, more than 20% of all sources in the cerebrum and cerebellum were affected; this means for 20% of the sources, the localization error was larger than 5 mm.

Discussion

In our study, we investigated the influence of a wide range of skull geometry deficiencies on EEG source analysis. A detailed, high resolution reference volume conductor model was employed. Error maps for forward and inverse errors were presented, and influences were characterized by their mislocalization tendency. Finally, all the influences, which were studied in an identical simulation setup, were compared.

Our results show that local defects in skull geometry (i.e., skull holes, local skull thickness misspecification or modeling sinuses as compact bone) only lead to forward and source reconstruction errors for sources in the immediate vicinity of the defect. Small defects, commonly resulting from segmentation procedures, for example, a skull hole with only 2 mm diameter or a thickness change of only 2 mm, caused negligible errors. Changes in skull geometry in a larger region of the volume conductor and close to the source space resulted in more distinct forward and inverse errors. This was observed in the models cut directly below the skull and the test models with simplified inferior skull or skull and scalp. Large changes of the volume conduction properties did not affect the forward simulations and the source reconstruction when the changes were introduced

in areas far away from the sensors and the source space. This was observable in test models 4b-d, where the skull was cut at 20 or 40 mm distance to the skull and where further simplifications were introduced in inferior parts of the volume conductor.

We investigated both the influence of skull geometry defects on the forward simulation of scalp potentials and the influence on source reconstruction. RDM and MAG errors, which we used to evaluate the forward simulation results, already provide an indication of how source analysis will be affected independent of the exact type of inverse procedure and source distribution (single versus multiple sources). However, these measures are quite abstract and cannot be directly related to source localization errors, which are of practical interest in most applications. The source reconstruction results presented allow a more explicit statement with regard to the expected source localization errors when performing source reconstruction in volume conductor models incorporating the skull geometry defects studied. However, one has to keep in mind that we examined source reconstruction in scenarios with single dipole sources and conclusions are therefore only valid for these scenarios. Localization errors in source scenarios with multiple active sources might be considerably larger.

We took care to construct a detailed and anatomically plausible reference volume conductor model, which, however, still has limitations as discussed in the following.

Some simplifications concerning the geometry of the skull in the reference model were necessary. As only MR data was available for the segmentation of the reference model, some uncertainty regarding the exact position and shape of the sinus cavities remains. Smaller sinus cavities would lead to smaller errors for test models 3a and b, where the sinus cavities were modeled as compact bone. In addition, holes through which nerves and blood vessels pass that are actually present in the skull base are not incorporated in our reference model. Only the holes for the eye nerves and the foramen magnum were modeled. We assume that incorporating the additional openings in the skull base would have resulted in additional errors of a local nature (similar to the results of test models

1a-c) for test models 5a to c and 6a to c, where the skull base is approximated as a closed layer of constant thickness thereby ignoring the openings.

Even if the conductivity of the CSF was reported to be very stable inter-individually (Baumann et al., 1997), other conductivity values might differ inter- and intra-individually. The variability for the compact bone tissue (Akhtari et al., 2002, Oostendorp et al., 2000) is especially relevant to this study and will thus be discussed in the following. It is to be expected that a higher compact bone conductivity that is closer to the conductivity of the surrounding tissues, for example, muscle, CSF or brain, will lead to smaller errors for nearly all test models, for example, when introducing erroneous skull holes or local errors in skull thickness. On the other hand, if the compact bone conductivity is smaller in reality, this will amplify nearly all reported effects. The test models where sinus cavities are modeled as compact bone are the only exception. Here, effects will be smaller when the compact bone conductivity is smaller than assumed here and larger when it is larger. These claims are supported by results of additional simulations that were performed using a by 28% higher compact bone conductivity (0.0064 S/m instead of 0.005 S/m). It was found that errors were only slightly smaller when increasing the compact bone conductivity. For test model 6c, for example, the proportion of affected sources with regard to the localization error only changed from 30.3% to 27.0%. Thus, we believe that the results presented here are representative, even if the exact value for the compact bone conductivity might not be known.

Another aspect in which our reference volume conductor is simplified is the modeling of WM conductivity. Because our study focused on the effects of skull modeling, WM was simplified using an isotropic conductivity value, whereas it is actually anisotropic, with higher conductivity along fibers and lower conductivity perpendicular to fibers. For the effect of WM anisotropy, see, for example, (Wolters et al., 2001, Haueisen et al., 2002, Güllmar et al., 2010). In the most recent investigation by Güllmar et al. (Güllmar et al., 2010), a median RDM error of 0.071 between the isotropic reference model and a model with 1:10 WM anisotropy was found. This error is large

enough to be important for EEG source analysis, but it is small enough for us to suspect that the characteristics of the potential distribution inside the volume conductor are not significantly altered, meaning that the results of our study would not change considerably if WM anisotropy were introduced into our reference volume conductor model.

For some of the skull geometry defects and simplifications, we can find comparable studies in the literature. In a previous study by Bénar et al. (Benar and Gotman, 2002), the influences of a skull hole on the EEG forward computations and source reconstruction were presented. The authors found that the errors in the forward simulation, caused by a hole added to the skull, are largest for sources close to the skull hole and decrease for sources at some distance to the hole. Our RDM error maps (Figure 3a) confirm this finding. We cannot directly compare our source reconstruction results to the results presented in the latter study, as their simulation study differs from the one presented here in one important aspect. Bénar et al. computed the reference data for their source reconstruction study in a reference model that incorporated a hole in the skull, and they used a model with intact skull geometry to reconstruct the sources from the reference data. This is contrary to our study design, where the model with the intact skull is the reference model. Bénar et al. reported that when using the model without skull holes, the sources were reconstructed too far towards the skull hole. This agrees with our finding that the sources reconstructed in the model incorporating a hole are reconstructed farther away from the hole (Figure 6a).

The influence of skull holes on source reconstruction from EEG data was also investigated by Vanrumste et al. (Vanrumste et al., 2000). Their error maps are in good agreement with the error maps presented in Figure 5a. However, the maximum localization error reported in their study for a hole of 20 mm diameter is only slightly larger than 5 mm, while it was larger than 9 mm for a hole with half the diameter in our study. This difference might be explained by the conductivity values chosen for the skull and for the skull hole. In our study, the ratio of skull hole conductivity to skull conductivity was 22 and therefore larger than in Vanrumste at al.'s study, where it was only

16.Local skull thickness changes were discussed by Cuffin (Cuffin, 1993), where localization errors well below 1 cm in volume conductor models with local variations in skull thickness were observed. Our results, with localization errors less than 5 mm for all probe sources, confirm Cuffin's observations.

Bruno et al. (Bruno et al., 2003) discussed the effect of the downward extension of the volume conductor model on the EEG forward simulations. They concluded that cutting the model at a cut plane which intersects the skull causes large errors in the simulated scalp potentials. This agrees with Figure 3e, where the forward errors for the model cut directly below the skull are presented. The authors furthermore reported that the errors decrease non-linearly when the model is extended further downwards. The RDM and localization errors we found for test models 4b and 4c confirm this finding.

Finally, we would like to put the model error investigated in this study into the context of other model errors reported in the literature. We can relate our results regarding the effects of skull geometry defects to Dannhauer et al.'s work (Dannhauer et al., 2011), where different ways of modeling the skull conductivity were investigated. Dannhauer et al. demonstrated that for widespread areas of the brain, large localization errors of 10 mm or more are expected when the three-layered skull is modeled as a single compartment with homogeneous isotropic conductivity. This is comparable to the influences we observed when cutting the model directly below the skull (test model 4a) or when approximating inferior skull (test models 5) or inferior skull and scalp (test models 6) as layers of constant thickness.

Yvert et al. (Yvert et al., 1997) investigated localization errors obtained when spherical instead of realistic volume conductor models were used for EEG source reconstruction, and found localization errors of 4-6 mm for sources in the upper part of the head and errors of 15-25 mm for sources in the lower part of the head. These errors are at least of the same order as the maximum errors in our study, which we found for test models 5a-c and 6a-c.

Conclusion

We investigated a wide variety of skull geometry defects and simplifications on EEG source analysis. The results of our study allow us to formulate guidelines for the construction of volume conductor models for EEG source analysis. The volume conductor model should be extended downwards at least 20, or even better 40 mm below the skull. It is acceptable to model the inferior part of the head (i.e., tissues more than 30 mm away from the source space) as scalp. Neither the inferior skull nor the inferior scalp, however, should be approximated as a layer of constant thickness. The complex geometry of the skull base should be taken into account as accurately as possible. Skull holes larger than 2 mm in diameter and errors in skull thickness should be avoided and frontal sinuses should be modeled as filled with air. However, all latter defects result in only local errors in the close vicinity of the defects. Therefore, in many studies, these defects can be ignored.

In a next step, automatic segmentation procedures for volume conductor generation should be designed and evaluated, taking these guidelines into account. These convenient automatic methods will facilitate the routine employment of accurate, individual, and realistic volume conductor models in EEG source analysis, and thereby improve reliability and accuracy of source analysis.

Acknowledgement

This work was kindly supported by the Deutsche Forschungsgemeinschaft (contract grant numbers WO 1425/1-1, WO 1425/2-1, JU 445/5-1, KN 588/2-1).

References

Abascal, J. F., Arridge, S. R., Atkinson, D., Horesh, R., Fabrizi, L., Lucia, M. D., Horesh, L., Bayford, R. H., and Holder, D. S. (2008). Use of anisotropic modelling in electrical impedance tomography; description of method and preliminary assessment of utility in imaging brain function in the adult human head. *Neuroimage*, 43(2):258–268.

Acar, Z. A. and Makeig, S. (2010). Neuroelectromagnetic forward head modeling toolbox. *Journal of Neuroscience Methods*, 190:258–270.

Akhtari, M., Bryant, H., Mamelak, A., Flynn, E., Heller, L., Shih, J., Mandelkem, M., Matlachov, A., Ranken, D., Best, E., et al. (2002). Conductivities of three-layer live human skull. *Brain Topography*, 14(3):151–167.

Awada, K., Jackson, D., Williams, J., Wilton, D., Baumann, S., and Papanicolaou, A. (1997). Computational aspects of finite element modeling in EEG source localization. *Biomedical Engineering, IEEE Transactions on*, 44(8):736–751.

Baumann, S., Wozny, D., Kelly, S., and Meno, F. (1997). The electrical conductivity of human cerebrospinal fluid at body temperature. *IEEE Transactions on Biomedical Engineering*, 44(3):220–223.

Benar, C. G. and Gotman, J. (2002). Modeling of post-surgical brain and skull defects in the EEG inverse problem with the boundary element method. *Clinical Neurophysiology*, 113(1):48–56.

Berg, P. and Scherg, M. (1994). A fast method for forward computation of multiple-shell spherical head models. *Electroencephalography and Clinical Neurophysiology*, 90(1):58–64.

Bertrand, O., Thévenet, M., and Perrin, F. (1991). 3D finite element method in brain electrical activity studies. In Nenonen, J., Rajala, H., and Katila, T., editors, *Biomagnetic Localization and 3D Modelling*, pages 154–171. Report of the Dep. of Tech.Physics, Helsinki University of Technology.

Bruno, P., Vatta, F., Mininel, S., and Inchingolo, P. (2003). Head model extension for the study of bioelectric phenomena. *Biomedical Sciences Instrumentation*, 39:59–64.

Bruno, P., Vatta, F., Mininel, S., and Inchingolo, P. (2004). Referenced EEG and head volume conductor model: geometry and parametrical setting. In *Engineering in Medicine and Biology Society, 2004. IEMBS '04. 26th Annual International Conference of the IEEE*, volume 1, pages 833–836.

Buchner, H., Knoll, G., Fuchs, M., Rienäcker, A., Beckmann, R., Wagner, M., Silny, J., and Pesch, J. (1997). Inverse localization of electric dipole current sources in finite element models of the human head. *Electroencephalography and Clinical Neurophysiology*, 102:267–278.

Cuffin, B. N. (1993). Effects of local variations in skull and scalp thickness on EEG's and MEG's. *IEEE Transactions on Biomedical Engineering*, 40(1):42–48.

Dannhauer, M., Lanfer, B., Wolters, C. H., and Knösche, T. R. (2011). Modelling of the human skull in EEG source analysis. *Human Brain Mapping*.

de Munck, J. (1988). The potential distribution in a layered anisotropic spheroidal volume conductor. *Journal of Applied Physics*, 64:465–469.

de Munck, J., van Dijk, B., and Spekreijse, H. (1988). Mathematical dipoles are adequate to describe realistic generators of human brain activity. *Biomedical Engineering, IEEE Transactions on*, 35(11):960–966.

Gencer, N. and Acar, C. (2004). Sensitivity of EEG and MEG measurements to tissue conductivity. *Phys.Med.Biol.*, 49:701–717.

Güllmar, D., Haueisen, J., and Reichenbach, J. (2010). Influence of anisotropic electrical conductivity in white matter tissue on the EEG/MEG forward and inverse solution. A high-resolution whole head simulation study. *NeuroImage*. doi:10.1016/j.neuroimage.2010.02.014.

Hallez, H., Vanrumste, B., Hese, P. V., D'Asseler, Y., Lemahieu, I., and de Walle, R. V. (2005). A finite difference method with reciprocity used to incorporate anisotropy in electroencephalogram dipole source localization. *Phys.Med.Biol.*, 50:3787–3806.

Hämäläinen, M., Hari, R., R.Ilmoniemi, Knuutila, J., and O.Lounasmaa (1993). Magnetoencephalography: theory, instrumentation, and applications to noninvasive studies of the working human brain. *Rev.Mod.Phys.*, 65:413–497.

Hartmann, U. and Berti, G. (2000-2003). VGRID: A fast and robust octree-based 3D mesh generator for unstructured grids. (SimBio Development Group, 2011).

Haueisen, J., Ramon, C., Czapski, P., and Eiselt, M. (1995). On the influence of volume currents and extended sources on neuromagnetic fields: A simulation study. *Annals of Biomedical Engineering*, 23(6):728–739.

Haueisen, J., Tuch, D. S., Ramon, C., Schimpf, P. H., Wedeen, V. J., George, J. S., and Belliveau, J. W. (2002). The influence of brain tissue anisotropy on human EEG and MEG. *NeuroImage*, 15(1):159–166.

Irimia, A. (2005). Electric field and potential calculation for a bioelectric current dipole in an ellipsoid. *Journal of Physics A: Mathematical and General*, 38(37):8123–8138.

Kaipio, J. and Somersalo, E. (2007). Statistical inverse problems: Discretization, model reduction and inverse crimes. *Journal of Computational and Applied Mathematics*, 198(2):493–504.

Kybic, J., Clerc, M., Abboud, T., Faugeras, O., Keriven, R., and Papadopoulo, T. (2005). A common formalism for the integral formulations of the forward EEG problem. *IEEE Transactions on Biomedical Imaging*, 24(1):12–18.

Law, S. (1993). Thickness and resistivity variations over the upper surface of the human skull. *Brain Topography*, 2:99–109.

Lew, S., Wolters, C., Dierkes, T., Röer, C., and MacLeod, R. (2009). Accuracy and run-time comparison for different potential approaches and iterative solvers in finite element method based EEG source analysis. *Applied Numerical Mathematics*, 59(8):1970–1988. http://dx.doi.org/10.1016/j.apnum.2009.02.006, NIHMSID 120338, PMCID: PMC2791331.

Li, J., Wang, K., Zhu, S., and He, B. (2007). Effects of holes on EEG forward solutions using a realistic geometry head model. *Journal of Neural Engineering*, 4(3):197–204.

Marin, G., Guerin, C., Baillet, S., Garnero, L., and G., M. (1998). Influence of skull anisotropy for the forward and inverse problem in EEG: simulation studies using the FEM on realistic head models. *Human Brain Mapping*, 6:250–269.

McVeigh, P., Bostan, A., and Cheyne, D. (2007). Study of conducting volume boundary influence on source localization using a realistic MEG phantom. *International Congress Series*, 1300:153–156.

Meijs, J., Weier, O., Peters, M., and van Oosterom, A. (1989). On the numerical accuracy of the boundary element method. *IEEE Transactions on Biomedical Engineering*, 36(10):1038–1049.

Nuwer, M. R., Comi, G., Emerson, R., Fuglsang-Frederiksen, A., GuÃƒÂ©rit, J., Hinrichs, H., Ikeda, A., Jose C. Luccas, F., and Rappelsburger, P. (1998). IFCN standards for digital recording of clinical EEG. *Electroencephalography and Clinical Neurophysiology*, 106(3):259–261.

Oostendorp, T. F., Delbeke, J., and Stegeman, D. F. (2000). The conductivity of the human skull: results of in vivo and in vitro measurements. *Biomedical Engineering, IEEE Transactions on*, 47(11):1487–1492.

Oostenveld, R. and Oostendorp, T. F. (2002). Validating the boundary element method for forward and inverse EEG computations in the presence of a hole in the skull. *Human Brain Mapping*, 17(3):179–192.

Plonsey, R. and Heppner, D. (1967). Considerations on quasi-stationarity in electro-physiological systems. *Bulleting of Mathematical Biology*, 29:657–664.

Ramon, C., Schimpf, P., Haueisen, J., Holmes, M., and Ishimaru, A. (2004). Role of soft bone, CSF and gray matter in EEG simulations. *Brain Topography*, 16(4):245–248.

Roche-Labarbe, N., Aarabi, A., Kongolo, G., Gondry-Jouet, C., Dümpelmann, M., Grebe, R., and Wallois, F. (2008). High-resolution electroencephalography and source localization in neonates. *Human Brain Mapping*, 29(2):167–176.

Rullmann, M., Anwander, A., Dannhauer, M., Warfield, S., Duffy, F., and Wolters, C. (2009). EEG source analysis of epileptiform activity using a 1 mm anisotropic hexahedra finite element head model. *NeuroImage*, 44(2):399–410.

Sadleir, R. and Argibay, A. (2007). Modeling skull electrical properties. *Ann.Biomed.Eng.*, 35(10):1699–1712.

Sarvas, J. (1987). Basic mathematical and electromagnetic concepts of the biomagnetic inverse problem. *Phys.Med.Biol.*, 32(1):11–22.

SCIRun (2011). : A scientific computing problem solving environment. Scientific Computing and Imaging Institute (SCI).

SimBio Development Group (2011). SimBio: A generic environment for bio-numerical simulations. online, https://www.mrt.uni-jena.de/simbio, accessed Jan 18.

Smith, S. M. (2002). Fast robust automated brain extraction. *Human Brain Mapping*, 17(3):143 – 155.

van den Broek, S. P., Reinders, F., Donderwinkel, M., and Peters, M. J. (1998). Volume conduction effects in EEG and MEG. *Electroencephalography and Clinical Neurophysiology*, 106(6):522–534.

Vanrumste, B., Hoey, G. V., de Walle, R. V., D'Have, M., Lemahieu, I., and Boon, P. (2000). Dipole location errors in electroencephalogram source analysis due to volume conductor model errors. *Medical and Biological Engineering and Computing*, 38(5):528–534.

Wells, W. M., Viola, P., Atsumi, H., Nakajima, S., and Kikinis, R. (1996). Multi-modal volume registration by maximization of mutual information. *Medical image analysis*, 1(1):35–51.

Wendel, K., Narra, N., Hannula, M., Kauppinen, P., and Malmivuo, J. (2008). The influence of CSF on EEG sensitivity distributions of multilayered head models. *IEEE Trans. Biomed. Eng.*, 55(4):1454–1456.

Wendel, K., Väisänen, O., Malmivuo, J., Gencer, N., Vanrumste, B., Durka, P., Magjarevic, R., Supek, S., Pascu, M., Fontenelle, H., et al. (2009). Eeg/meg source imaging: methods, challenges, and open issues. *Computational intelligence and neuroscience*, 2009:13.

Wolters, C., Anwander, A., Koch, M., Reitzinger, S., Kuhn, M., and Svensén, M. (2001). Influence of head tissue conductivity anisotropy on human EEG and MEG using fast high resolution finite element modeling, based on a parallel algebraic multigrid solver. In Plesser, T. and Macho, V., editors, *Contributions to the Heinz-Billing Award*, number 58, pages 111–157. Gesellschaft für wissenschaftliche Datenverarbeitung mbH Göttingen. ISSN: 0176-2516, http://www.billingpreis.mpg.de.

Wolters, C., Köstler, H., Möller, C., Härtlein, J., Grasedyck, L., and Hackbusch, W. (2007a). Numerical mathematics of the subtraction method for the modeling of a current dipole in EEG source reconstruction using finite element head models. *SIAM Journal on Scientific Computing*, 30(1):24–45.

Wolters, C. H., Anwander, A., Berti, G., and Hartmann, U. (2007b). Geometry-adapted hexahedral meshes improve accuracy of finite element method based EEG source analysis. *IEEE Transactions on Biomedical Engineering*, 54(8):1446–1453.

Wolters, C. H., Grasedyck, L., and Hackbusch, W. (2004). Efficient computation of lead field bases and influence matrix for the FEM-based EEG and MEG inverse problem. *Inverse Problems*, 20(4):1099–1116.

Yan, Y., Nunez, P. L., and Hart, R. T. (1991). Finite-element model of the human head: scalp potentials due to dipole sources. *Medical and Biological Engineering and Computing*, 29(5):475 – 481.

Yvert, B., Bertrand, O., Thévenet, M., Echallier, J. F., and Pernier, J. (1997). A systematic evaluation of the spherical model accuracy in EEG dipole localization. *Electroencephalography and Clinical Neurophysiology*, 102(5):452–459.

Zhang, Y., Brady, M., and Smith, S. (2001). Segmentation of brain MR images through a hidden Markov random field model and the expectation-maximization algorithm. *Medical Imaging, IEEE Transactions on*, 20(1):45–57.

Supplementary Material

In this document we present supplementary material, which might additionally be of interest.

Additional error plots

In line with our investigations also the magnitude error (MAG) was evaluated. MAG error maps for selected test models are shown in Figure A 1, demonstrating for which sources the potential is overestimated (MAG > 1) and for which sources the potentials in the test models is underestimated (MAG < 1).

Figure 6 in the article presents the mislocalization tendencies for reference sources distributed on a 10 mm regular grid covering the entire source space. At each node of the grid, 10 reference sources are placed with varying orientations evenly distributed across one hemisphere. For the creation of the error maps in Figure 6 the mislocalization vectors are averaged across all orientations. For single orientations the mislocalization might be substantially larger than the averaged ones. Therefore, we additionally provide Figure A 2 here. In Figure A 2 the mislocalization for the dipole source orientation having the largest localization error is shown. The comparison of these error maps with Figure 6 of the article gives insight into the variance of the localization errors depending on the source orientation.

Also of interest to the reader might be a differentiation between the forward and inverse errors for sources in the whole brain and the errors for sources only in the cerebrum. Figures 4 and 7 in the article already show the mean and maximum errors, as well as the proportion of affected sources, with respect to sources throughout the complete source space. Figures A3 and A4 show in addition the error characteristics for sources in the cerebrum only.

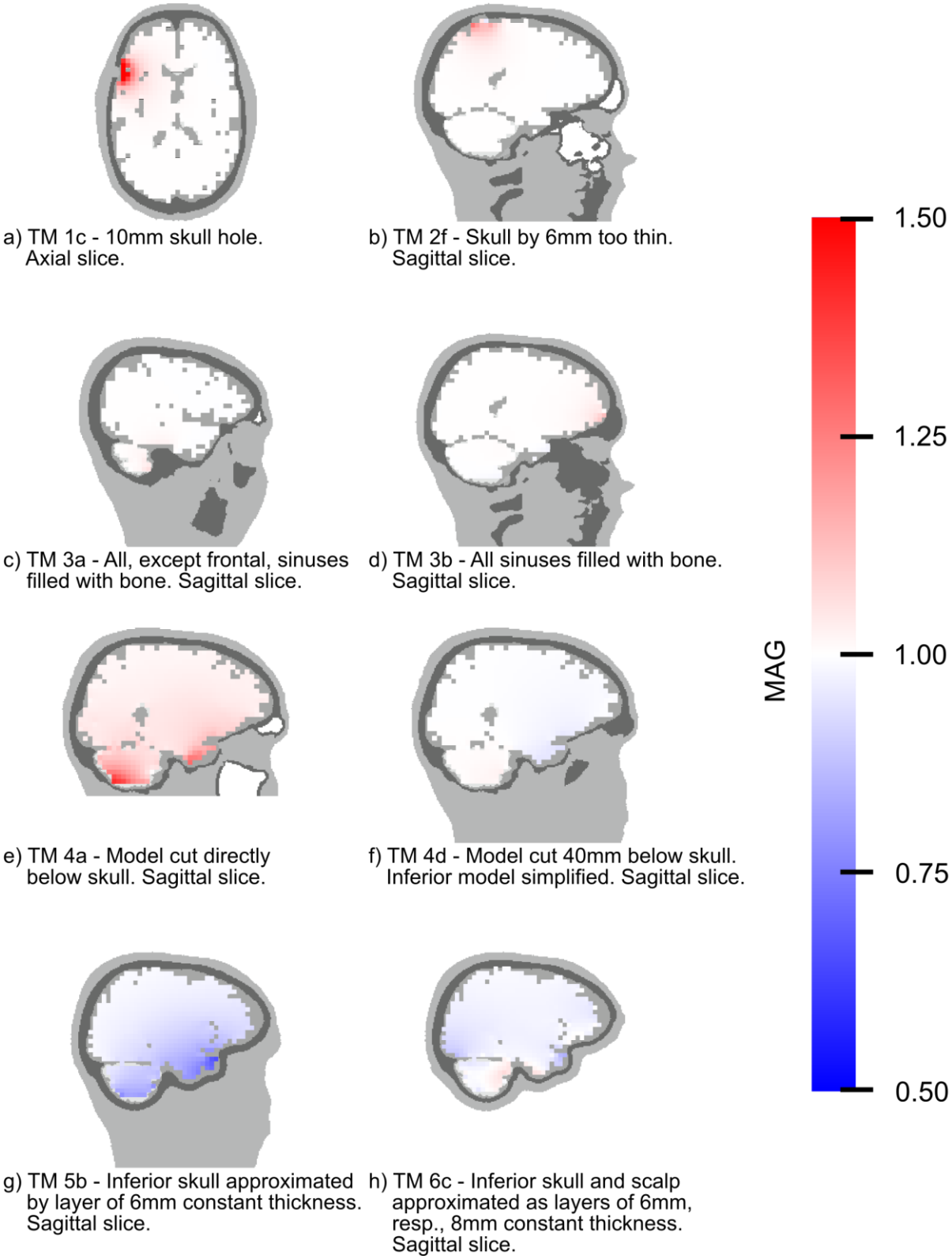

Figure A 1 MAG error maps for selected test models. Errors for sources at the same position, but with different orientations were averaged.

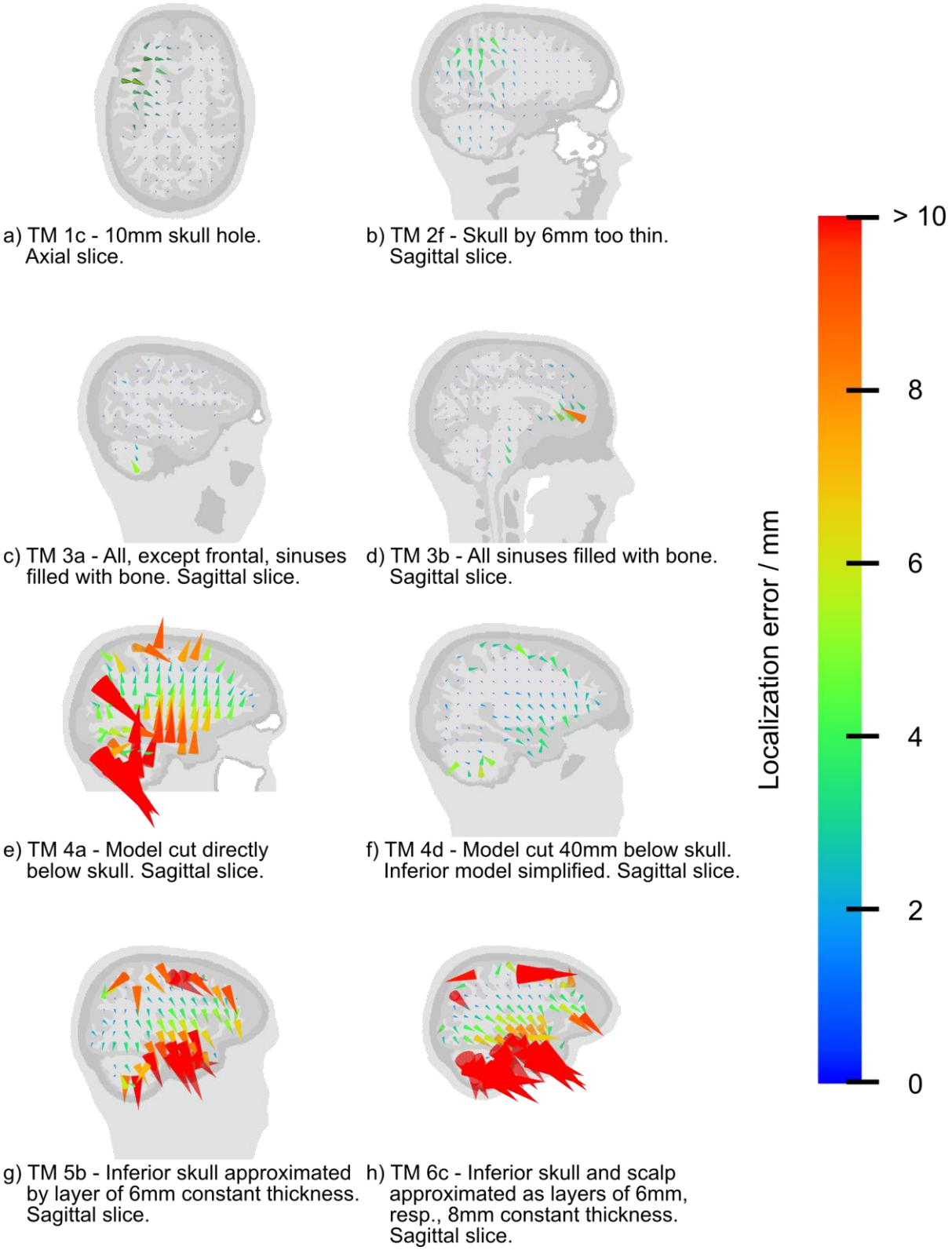

Figure A 2 Maps showing mislocalization for the reference source direction with maximum localization error. Cones point from the reference source position towards the reconstructed source position. Maps are shown for selected test models. The length of the cones is scaled by a factor of 3 to improve visibility of small mislocalizations. Presented mislocalizations are capped at 20mm for improved clarity.

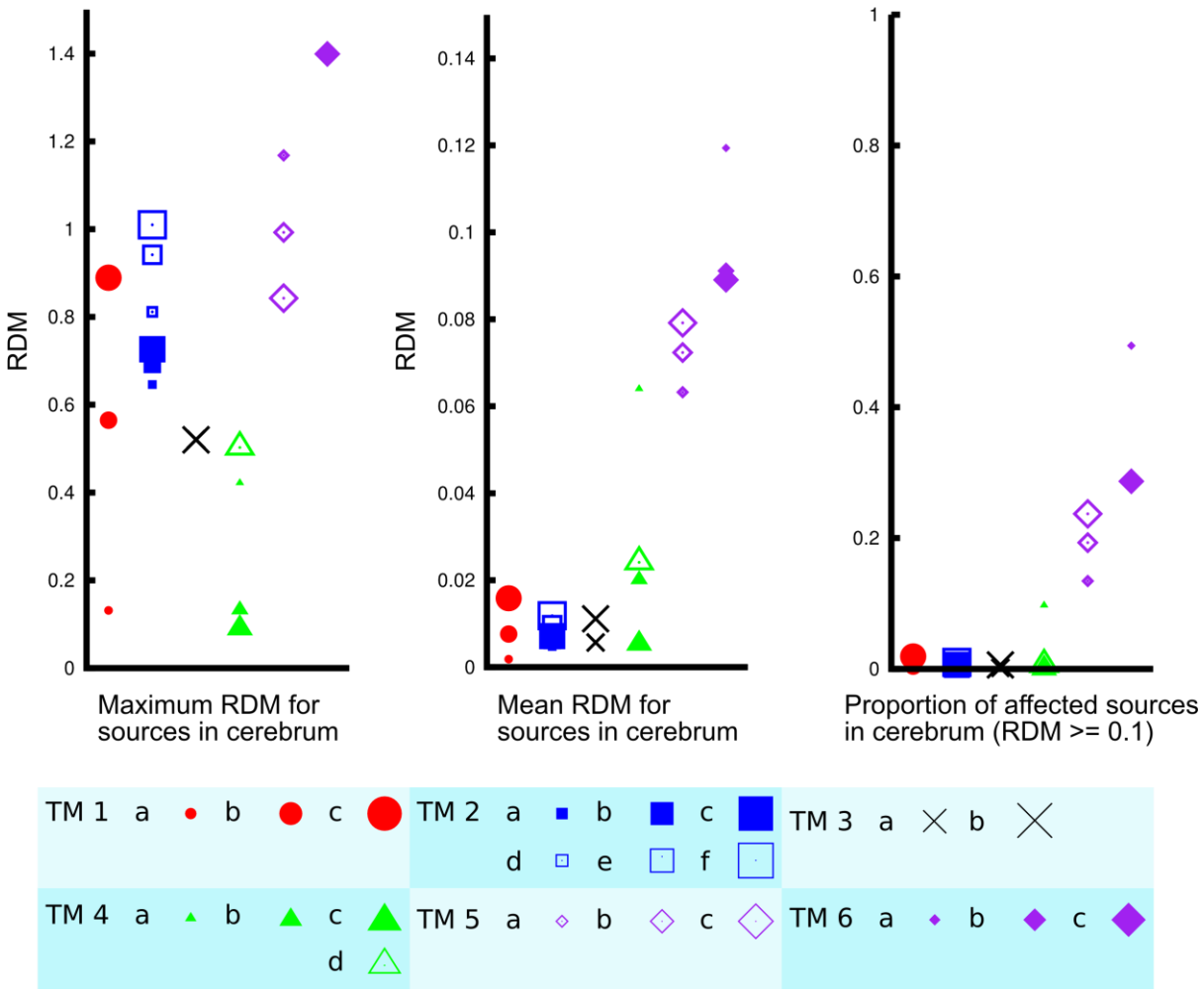

Figure A 3 RDM error characteristics for sources in cerebrum only.

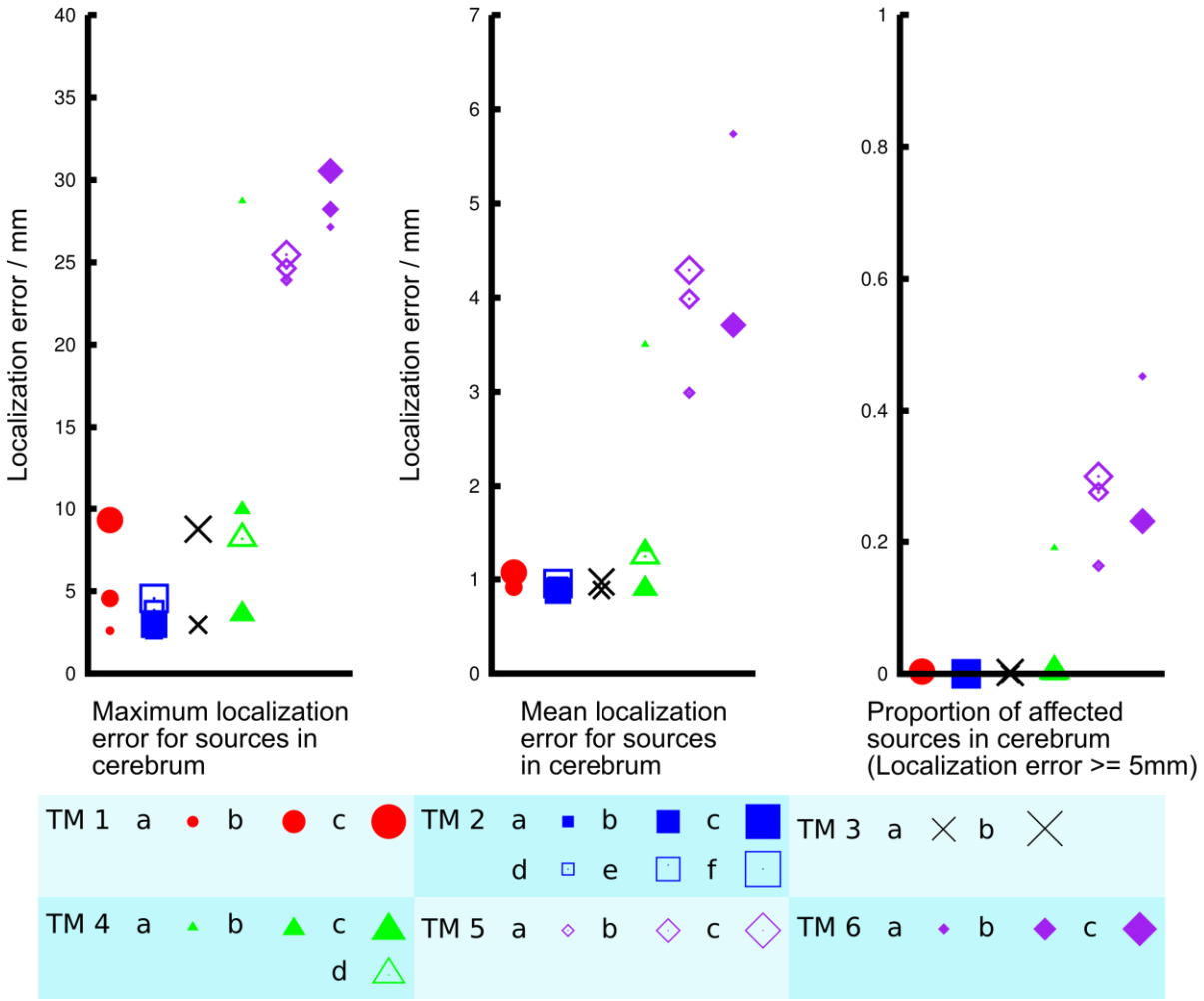

Figure A 4 Localization error characteristics for sources in cerebrum only.